Received December 15, 2023, accepted July 17 2024, date of publication July 25 2024.

Deep Learning and Photoacoustic Technology for Microcirculation Classification: Comparison Between Smoking and Nonsmoking Groups

Hui Ling Chua and Audrey Huong

Department of Electronic Engineering, Universiti Tun Hussein Onn Malaysia, Parit Raja, Johor

ABSTRACT

Abstract: Smoking has a significant impact on microcirculation, but existing tools for monitoring circulation perfusion in the smoking group have different shortcomings. This preliminary study explores the feasibility of using an in-house assembled multispectral photoacoustic (PA) system to investigate and compare the microcirculation performance between smoking and nonsmoking subjects. For this purpose, pretrained Alexnet, Long Short-Term Memory (LSTM), and a hybrid Alexnet-LSTM network were employed for the prediction task. This research included five smoking and thirty-two nonsmoking participants in the investigations that involved two experimental conditions, i.e., at rest and arterial blood flow occlusion. The findings showed that the PA signals produced in the smoking group have generally smaller magnitudes and negligible differences (when comparing between the two experiment conditions) than their nonsmoking counterpart. The employed models performed superiorly with the highest accuracy of 90 % given by the hybrid model, followed by 80 % recorded for Alexnet and LSTM using nonsmoking data. The performance of these models is reduced when they are trained and tested using smoking data. Our study highlights the task complexity and difficulty in determining tissue microcirculation status in heavy smoking individuals, which has been attributed to their possibly pre-existing atherosclerotic conditions and the high carboxyhemoglobin (COHb) level. A longitudinal study of smoking habit-dependent microcirculation abnormalities in smokers could offer further avenues for investigation. Future research includes incorporating systematic experimental protocols and access to the participant's medical records to improve the performance of the clinical decision-making system used for field applications.

Keywords – *Microcirculation perfusion; photoacoustic; smoking; Alexnet; LSTM*

INTRODUCTION

Smoking increases the risks of various conditions, including lung cancer, heart disease, respiratory problems, and other significant health issues. It induces vasoconstriction, narrowing the blood vessels in microcirculation and reducing blood flow to organs and tissues. Consequently, oxygen delivery to the tissues is diminished, impairing their proper function. Smoking also increases blood viscosity, hindering nutrient and oxygen delivery through narrow microvessels; it promotes the formation of blood clots, obstructs microcirculatory vessels, and damages tissue. Tobacco smoke contains carbon monoxide (CO) as one of its toxic components. When tobacco is burned and inhaled, CO is absorbed into the bloodstream, significantly affecting microcirculation. CO causes adverse effects in humans by combining with hemoglobin to form carboxyhemoglobin (COHb), preventing blood from carrying oxygen.[1-2] Based on the reports of Silva,[3] there exists a close association between tobacco use and microvascular dysfunction, which is manifested by impeded blood flow.

Conventional technologies available to investigate microcirculation in the smoking population include Magnetic Resonance Imaging (MRI),[4] Pulse CO-oximetry,[5] and spectroscopy.[6–7] However, the use of MRI is limited because of its high operational cost and rigid working conditions. Investigation of microcirculatory performances based on tissue gas saturation using CO-oximeter and spectroscopy is limited by the light penetration depth and variable degree of light scattering from tissue heterogeneity.[8] Photoacoustic (PA) imaging, which combines the features of optical spectroscopy and deep penetration of acoustic technologies, has gained increasing interest as an alternative method in microcirculation flow abnormalities detection. The light illuminating a sample absorbed by chromophores in the skin produces thermal expansion, which generates acoustic waves that a transducer can detect. The peaks of PA signals are linearly associated with the sample properties, while the temporal characteristic of PA signals would disclose the physiological properties of the tissues. Traditionally, physicians, particularly radiologists, would review and examine medical images before deciding on treatment planning. These tasks are crucial in diagnostic radiography, involving challenging analysis and diagnosis based on visual images. Artificial Intelligence (AI) has become essential in assisting and enhancing these decision-making processes by providing accurate, reliable, and efficient interpretation of results. This technology has been actively studied for different PA applications; some recent AI efforts include Sumit et al. [9], who demonstrated using deep learning (U-Net model) for multi-target detection with simulated PA imaging datasets. Warrier et al.[10]combined optimization and deep learning approaches for detecting and classifying cancer tissues using multispectral PA imaging. The study by Mohajerani et al.[11] proposed a novel machine learning-empowered optoacoustic sensor for recognizing diabetes with different complications based on the signals recorded from phantom and skin surfaces (in the human experiments). The adopted machine learning approach used bagged ensemble trees to find the correlation and best fit between the data and its labels. Similar works were carried out by Liakat et al.[12] and Sei et al.[13]; the former developed an in-vivo noninvasive glucose sensor to predict glucose concentration using the least square regression technique and based on the photoacoustic measurement in the skin, whereas the latter study used regression technique to determine blood saturation using PA signals of blood samples.

To the authors' best knowledge, no works have been carried out to use deep learning and PA techniques to compare the microcirculation changes or flow abnormalities between smoking and nonsmoking subjects. This work aims to investigate and compare the performance of different deep learning models for microcirculatory status (i.e., during at-rest and perfusion occlusion in smoking and nonsmoking groups) classification using the PA method. All the computations were performed on a DELL laptop with 64-bit Windows 10, Intel® Xeon™ i7-1700M CPU @3.20 GHz. All simulations were done in MATLAB (2022b).

METHODS

Ethical statements: This study was approved by the local research ethics committee at Universiti Tun Hussein Onn Malaysia (RMC.100-9/139,4).

2.1 Photoacoustic (PA) detection system

The schematic diagram of the experimental setup is shown in Figure 1 (top). The illumination system consisted of two 5 mm ultra-bright transparent white light emitting diodes (model: 5LED-UL-W) filtered by color filters (model: FKB-VIS-10, Thorlabs) to generate five primary colors with a center light wavelength of 450 nm, 500 nm, 550 nm, 600 nm, and 650 nm. These wavelengths were selected as they encompass the absorption spectra of hemoglobin (i.e., oxyhemoglobin and deoxyhemoglobin) required for analysis. The light modulation for illumination of the target area was achieved using an Acousto Optic Modulator (AOM) controlled by a radiofrequency (RF) driver with a carrier frequency of 15 MHz. The AOM produced modulating signals required to illuminate the subject. The acoustic energy generated in the medium was detected using an ultrasonic flaw detector (EPOCH 650, Olympus Corp, Japan). A wideband bandpass filter with fixed cut-off frequencies (0.5–4 MHz) built into the flaw detector was used to filter out high-frequency noise. Figure 1 (bottom) shows the actual setup in the laboratory. During measurements, a transducer head was placed in contact with the skin, and acoustic gel was the coupling medium. The signals were recorded using the EPOCH 650 flaw detector for offline analysis.

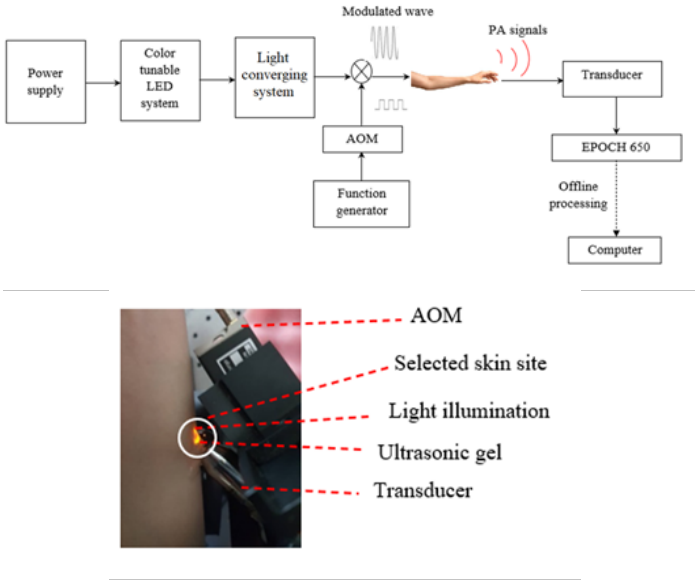

FIGURE 1. Schematic diagram of the PA system experiment setup (top) and a photograph of a color-tunable LED illuminating a subject's forearm during the measurement (bottom).

2.2 Subjects and protocol

Thirty-seven healthy individuals (19 males and 18 females, aged 21-30 years) were invited to participate in this research study. Among them, 32 were nonsmoking, and five were smoking participants, whose number of cigarette smoking years ranged from two to five years. The number of cigarettes smoked was between five to fifteen cigarettes a week. The local research ethics committee at Universiti Tun Hussein Onn Malaysia approved the study protocol (RMC.100-9/139,4). Before the study, these participants reported no known illnesses and were provided information about the experimental procedures, objectives, and potential risks. Upon enrolment, they provided their informed consent by signing a printed form. The experiment was conducted under two conditions: at rest and brachial artery blood flow occlusion to represent varying microcirculatory states.

The study commenced with the at rest experiment, where each participant was instructed to position the selected site beneath the illuminated light beam, starting with the light wavelength of 450 nm. The distance was maintained at 1 cm, and the angle of incidence was set at 45° from the source, as depicted in Figure 1 (bottom). Five signals were recorded from the same target site before varying the incident light wavelength. During the systolic occlusion experiment, a blood pressure cuff (model no. CK-110) was applied to the participants' upper left arm, i.e., by exerting a pressure of 140 mmHg for 30 seconds to induce ischemia, before the same data collection protocol was repeated. Inflating the cuff around the arm temporarily blocked blood flow, inducing an ischemic state in tissues below the cuff. This process promotes changes in the functional microcirculation by reducing the supply of oxygen-carrying blood to the lower extremities. This produces pathological conditions similar in patients with peripheral artery and vascular diseases. These procedures were applied to both smoking and nonsmoking (as the control group) individuals. The recorded screenshot signals were saved onto a microSD memory card using the flaw detector's built-in function for subsequent offline processing and analysis.

2.3 Signal pre-processing and dataset handling

Even though the produced PA signals are in 1D time series, the EPOCH 650 device has no function to save the raw signals. Therefore, a signal restoration approach was employed to convert the screenshot of the image saved on a microSD card into a vector representation or matrix format suitable for use with a time-based deep neural network (i.e., LSTM). This was facilitated by leveraging the distinct color contrast in the image, wherein the measured signal is depicted in green against a dark background. The image was first converted into a binary image using the im2bw function before the 1D matrix was obtained from the rows and columns of the image. The PA signal, X, from each measurement is of size 1 × 494 (i.e., X_1 …, X_{494}), which was fed into the network input layer for further classification and analysis.

The original PA signals did not provide a satisfactory result in the pre-experiment investigations using the LSTM network. Therefore, time-dependent moments were used. The moments' extraction is by using the tfsmoment function, and this study considered signal variance (order, n=2), skewness (n=3), and kurtosis (n=4) as the input features in the prediction of microcirculation status. The smoking PA images and the corresponding moments were randomly divided into a 40/20/40 % split for training, validation, and testing sets, rendering 20/10/20 images for convolutional-based models and 60/30/60 signals for the LSTM network. The nonsmoking dataset divided using the split ratio of 46/28/26 % giving 160/100/90 images and 480/300/270 signals used for convolutional-based models and LSTM, respectively.

2.4 Deep learning networks and model training

This study recruited pre-trained Alexnet, LSTM, and a hybrid model for microcirculation flow abnormalities classification based on the measured PA signal. AlexNet and the hybrid model take color (RGB) images as the input, while the moments calculated from 1D PA signal in section 2.3 is used as the input of LSTM. Modification and the use of these models are described in sections 2.4.1 and 2.4.2; these models were optimized for the problem by searching for the best hyperparameter settings in section 2.4.3.

2.4.1 Convolutional-based models

The convolutional-based models used in this work comprised the pretrained Alexnet and hybrid CNN-LSTM model shown in Figures 2 and 3. The input of these models was changed to 494 × 329 × 3, consistent with the original PA image size recorded from the system.

In Alexnet, the network's last fully connected (FC) was modified to two neurons representing: "0" for the normal class and "1" for the pathological (or abnormal) class. A dropout layer of 0.50 was placed between each FC layer in Figure 2 to reduce network overfitting. Meanwhile, the Alexnet-LSTM shown in Figure 3 was proposed to extract spatial and temporal features from the screenshot PA images. A batch normalization layer is added to this hybrid model to normalize inputs for the subsequent layer. The upper layers of this architecture (i.e., Alexnet) are to extract spatial information from the input image. The extracted abstract information is passed through a flattened layer, converting the feature map into one-dimensional data. This sequential data is fed into the LSTM network to extract the temporal patterns. This time-recurrent network consists of 500 hidden layers, which was decided

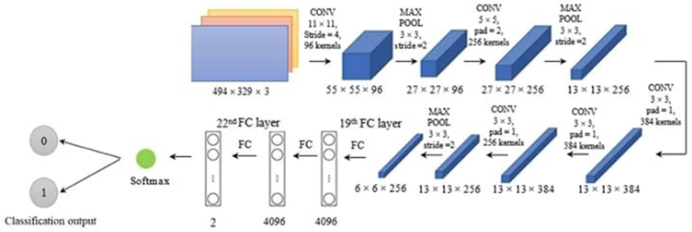

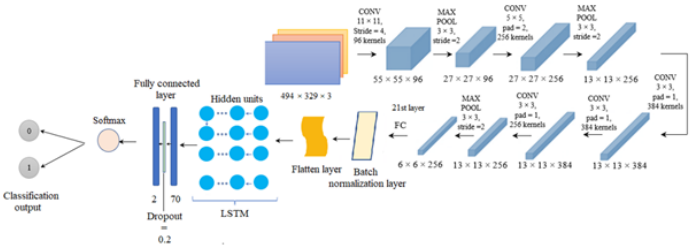

during pre-experiment tests. These layers are connected to FC layers and dropout layers of 0.2 to improve model generalization. The output of the FCs is fed to a Softmax to calculate class probabilities.

FIGURE 2. Architecture of Alexnet model.

FIGURE 3. Architecture of the proposed hybrid Alexnet-LSTM model.

2.4.2 Time-based deep neural network

The temporal recursive network, LSTM, was also chosen for the task due to its adeptness in handling sequential data and addressing short-term memory challenges. Its architecture consists of an input layer, taking the calculated moment features described in section 2.2 as the input signals, followed by a sequence of 155 hidden layers to extract their essential temporal features. These are followed by six FC layers, whose sizes progressively decrease from 40 to 30, 20, 10, 5, 3, and 2. While no definitive method for determining FC sizes exists, this study adopted a diminishing sequence to simplify the model's structure, as shown in Figure 4. A dropout layer with a value of 0.1 is incorporated after each FC layer to prevent the risk of overfitting, except for the final layer. The output from the final FC layers is fed into a Softmax classifier to classify a signal into two categories (i.e., 0: normal and 1: pathological condition).

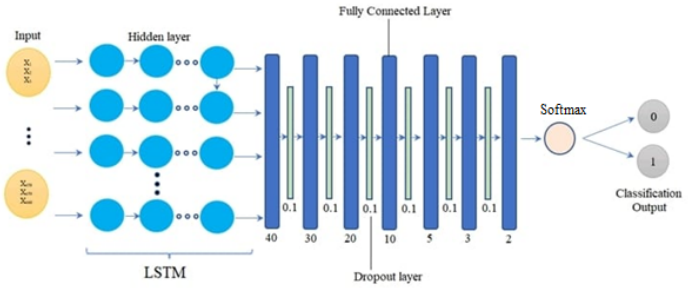

FIGURE 4. Architecture of the LSTM model.

2.4.3 Hyperparameters selection and model training

The classification models in Figures 2–4 were trained using the ADAM optimizer, known for its fast computation and quick convergence, while other important hyperparameters in Table 1 were adjusted manually.

TABLE 1. The Tuning Range of the Considered Hyperparameters and the Chosen Values

Parameter	Models	Limit		Step of change	Optimum hyperparameter
		Lower	Upper		
Epoch number	Alexnet	1	100	10	50
	LSTM	1	4000	100	500
	Hybrid	1	100	10	50
Mini Batch size	Alexnet	2	128	2^n, where n = 2,3...7	16
	LSTM	2	2048	2^n, where n = 2,3...11	32
	Hybrid	2	128	2^n, where n = 2,3...7	16
Initial learning rate	Alexnet LSTM Hybrid	5 × 10-4	1	5 × 10-4	5 × 10-4
Gradient descent threshold	Alexnet LSTM Hybrid	1×10^{-3}	1	$1e^{-n}$, n = 3, 2, 1, 0	1×10^{-3}

The optimal hyperparameters setting differed depending on the datasets and models used. Two-hundred sets of combinations consisting of different values in Table 1 were attempted in search for the best hyperparameters. The prediction accuracy fluctuated between 19% and 100%, while the training times varied from 56 to 154 minutes. This study identified the best combination based on the set that produced the highest training accuracy, such as 100 % for data of all wavelengths. The same optimum hyperparameters setting {epoch no., minibatch size, learning rate and gradient threshold} has been found for Alexnet and hybrid model as {50, 16, 0.0005, and 0.001} and {70, 16, 0.0001, and 0.001}, respectively, for smoking and nonsmoking data, and {500, 32, 0.0005, and 0.001} and {3000, 256, 0.0001, and 0.001}, respectively, for LSTM.

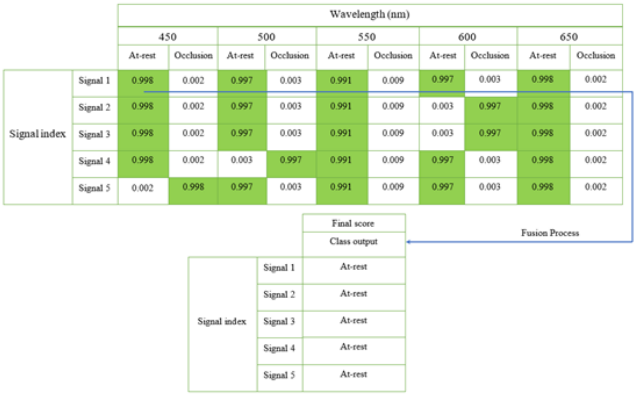

2.5 Score fusion strategy

This study used a combined prediction score to enhance the system's classification confidence. The class probability from models trained with each wavelength (i.e., 450 to 650 nm) was combined through summing to give the final score. This strategy is coined as the fusion method. An example of the fusion technique is shown in Figure 5.

FIGURE 5. Fusion technique for final classification of microcirculatory status.

2.6 Performance metric

The effectiveness of the trained models used in this study is evaluated using classification accuracy shown in Equation (1). This performance metric measures the degree of closeness of predictions to actual values.

$$\text{Accuracy} = \frac{\sum_{i=1}^{T} \frac{TP_i + TN_i}{TP_i + TN_i + FP_i + FN_i}}{N} \quad (1)$$

T denotes the total number of data and N denotes the total number of class labels ($N = 2$). A true positive (TPi) is when the abnormality for signal i is correctly detected. A false positive (FP) is the percentage of normal data misclassified as abnormal, a false negative (FN) is an abnormal signal class member incorrectly classified as normal, and a true negative (TN) is the correct prediction of normal PA signal.

RESULTS

Smoking individuals are known for having a high risk for vascular diseases; thus, the blood occlusion procedure is applied to these individuals to allow investigation of system sensitivity in this group of populations. Figure 6 compares the peak of PA signals at different wavelengths for smokers and nonsmokers under at-rest and occlusion conditions. It can be observed that the PA signals from nonsmoking subjects have overall higher amplitude values under both at-rest and occlusion conditions as compared to smoking subjects.

The PA produced from both (smoking and nonsmoking) groups exhibit the same pattern. The signals produced

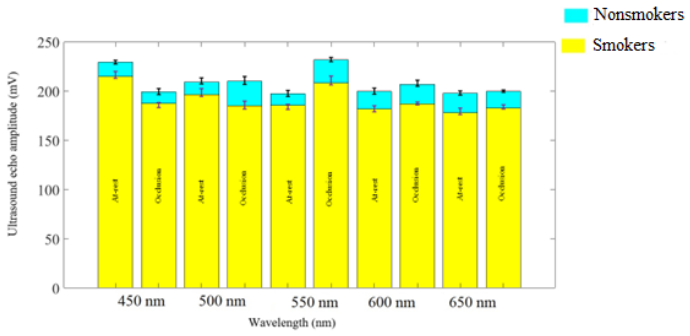

FIGURE 6. Mean and standard deviation (represented by error bar) of PA echo amplitudes produced in smokers and nonsmokers under different illumination wavelengths.

under at-rest and occlusion conditions peak at 450 nm and 550 nm, respectively, and the differences (between the different experimental conditions) are considerably negligible for wavelengths 500 nm, 600 nm, and 650 nm, as shown in the figure.

The classification results following the fine-tuning of the employed models using the nonsmoking and smoking data and from score fusion technique are shown in Figures 7 and 8, respectively. The training and testing of the Alexnet and hybrid model used screenshot images, while signal moments described in section 2.3 are used as the input to the LSTM.

DISCUSSION

PA technologies, such as skin glucose and oxygen saturation detections, have been extensively tested in various

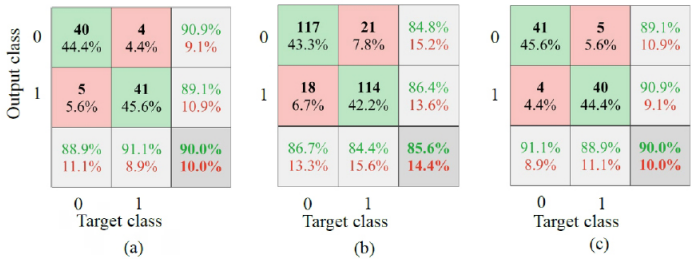

FIGURE 7. Confusion matrix of (a) Alexnet, (b) LSTM, and (c) hybrid model in classifying microcirculation status in nonsmoking subjects based on PA images and signals (class 0: normal, 1: abnormal).

FIGURE 8. Confusion matrix of (a) Alexnet, (b) LSTM, and (c) hybrid model for classification of microcirculation status (class 0: normal, 1: abnormal) in smokers based on PA images and signals.

diagnostic imaging applications. However, the use of this technology in the detection of compromised microcirculation, especially in the smoking population, has not been investigated. This research compares changes in blood perfusion under induced pressure in individuals with

different smoking habits based on PA signals produced under visible wavelengths illumination.

The fundamental principle of the adopted PA technology is that the magnitude of the PA signal produced by tissue depends on the hemoglobin variants' absorption properties, wherein the oxyhemoglobin light absorption peaks at 450 nm[14] while deoxyhemoglobin absorption peaks at 550–560 nm.[15] The absorption properties of these hemoglobin variants are similar for the remainder employed wavelengths (i.e., 500, 600, 650 nm). This trend was observed in Figure 6. This diagram revealed the highest PA signal magnitude recorded at 450 nm illumination, while 550 nm produced, generally, the highest ultrasonic echo amplitude under blood flow occlusion condition, where the regional tissue deoxygenated blood is rich due to impeded oxygen-carrying blood from flowing into the lower arm (measurement site). The PA signals obtained from smokers have considerably weaker echoes than nonsmokers, with a mean relative percent difference of 9.5% across all wavelengths and experiment conditions. This relative percent difference between nonsmoking and smoking results is divided by the two results. There is also high consistency in PA signals obtained from smoking subjects for both experiments. The COHb level is generally high in smokers, and the absorption spectrum of this hemoglobin variant, associated with the risk of inadequate oxygen delivery,[16] is considerably less prominent as it overlaps with that of oxyhemoglobin and deoxyhemoglobin in the visible wavelength range. While the dominance of light absorption of COHb could be the primary cause of the observations on the lower magnitude in the produced signals, we do not rule out the possibility of the already impaired microcirculation function or pre-existing atherosclerotic conditions in this group of participants, causing negligible differences in the readings between the at rest and external exerting pressure experiment.

Figure 7 shows the models' classification performance tested on nonsmoking (healthy) participants. The networks trained and tested on healthy subjects' data revealed considerably good accuracies ranging between 85.6 and 90%, suggesting the consistent performance between the convolutional-based models and temporal-based LSTM, and their feasibility in classifying normal and abnormal (occluded) microcirculation performance in nonsmoking individuals. Meanwhile, the results in Figure 8 reveal that the performance of these models decreased in the compromised microcirculation status (i.e., occlusion condition) detection. Even though the hybrid model achieved consistent classification accuracy (i.e., 90%), followed by Alexnet and LSTM with a classification accuracy of 80%, this group's FN rate is high (~20-40%). An investigation was carried out on the misclassified data, and it was found that they belong to the same subject, who reportedly smokes about fifteen cigarettes a week. All signals from this subject, the heaviest smoker among the five recruits, were misclassified as normal. One possible reason is that the atherosclerotic conditions, one of the known complications in smokers, could have been detected during at-rest condition, so further exerting external pressure on the limb during the blood occlusion experiment produced near negligible changes, as observed in the smoking group in Figure 6.

For the above-stated reasons, this work does not rule out the possibility of the models is overfitting to the normal (i.e., at rest) class in the smoking group, largely due to the negligible differences in the PA signals between at rest and occlusion conditions, compromising the classification performance of the models. Although an insufficient dataset (i.e., in the smoking group) could lead to biased predictions, the good performance of the models using nonsmoking data in Figure 7 and the high misclassification rates of pathological condition (i.e., between 20-40 %) that agreed well with the observations of,[17] and[18] indicating a certain degree of reliability of our findings.

It must also be mentioned that this study has no access to the participants' information, such as previous health records, and has not included their diet and environmental factors in the experimental design; these factors may influence the results and analyses of the study. Therefore, the future of this study includes recruiting more participants with various backgrounds and smoking habits and adopting a systematic experimental procedure (e.g., convenient access to patient's medical records) to investigate the blood microcirculatory performance between healthy and unhealthy (or patient) groups to enhance the validity

of the research findings. The improved clinical decision-making system can be integrated into the proposed PA system and considered an alternative imaging tool to facilitate the investigation of tumor angiogenesis and microvascular dysfunction, allowing early identification of compromised microcirculation and preventing further complications.

CONCLUSION

This paper demonstrated the use of deep learning-incorporated PA technology to investigate blood perfusion in nonsmoking and smoking subjects. The results showed that the proposed hybrid Alexnet-LSTM model performed better than the conventional Alexnet and LSTM models in the classification of microcirculation changes in both smoking and nonsmoking groups. These models performed inferiorly with high misclassification rates of 20–40% in the detection of compromised perfusion in the smoking group. This observation is attributed to the compromised perfusion in this group of subjects. This explains the negligible change observed after exerting external pressure impeding the (oxygen-carrying) blood flow and the limited smoking dataset for training the models. Future works include recruiting volunteers of diverse backgrounds, profiles, and smoking status to enhance the validity and practical application of existing findings in the healthcare system.

CONFLICTS OF INTEREST

No potential conflict of interest relevant to this article was reported.

FUNDING

Ministry of Higher Education (MOHE) Malaysia through Fundamental Research Grant Scheme (FRGS/1/2020/TK0/UTHM/02/28)

REFERENCES

1. Prockop, LD and Chichkova, RI. Carbon monoxide intoxication: an updated review. J Neurol Sci 2007;262:122–130. doi: 10.1016/j.jns.2007.06.037.
2. Fagerstrom, KO. Effects of a nicotine-enriched cigarette on nicotine titration, daily cigarette consumption, and levels of carbon monoxide, cotinine, and nicotine. Psychopharmacol (Berl) 1982;77:164–167. doi: 10.1007/BF00431941.
3. Silva H. Tobacco use and periodontal disease—the role of microvascular dysfunction. Microcirc Health Disease 2021;10(5): 441. doi: 10.3390/biology10050441
4. Chen NC, Chang WN, Lui CC, et al. Detection of gray matter damage using brain MRI and SPECT in carbon monoxide intoxication: a comparison study with neuropsychological correlation. Clin Nuclear Med 2013;38:e53-e59. doi: 10.1097/RLU.0b013e31827082a7.
5. Ozcan N, Ozcam G, Kosar P, et al. Correlation of computed tomography, magnetic resonance imaging and clinical outcome in acute carbon monoxide poisoning. Rev Bras Anestesiol 2016;66:529–532. doi: 10.1016/j.bjane.2014.05.006.
6. Parks J and Worth HG. Carboxyhemoglobin determination by second-derivative spectroscopy. Clin Chem 1985;31:279–281.
7. Huong AKC, Mahmud WMH, Tay KG, et al. Smoking status classification by optical spectroscopy and partial least square regression, J Physics: Conference Series 2019;1372:012031. doi: 10.1088/1742-6596/1372/1/012031.
8. Culnan DM, B. Craft-Cffman B, Bitz GH, et al. Carbon monoxide and cyanide poisoning in the burned pregnant patient: an indication for hyperbaric oxygen therapy. Ann Plast Surg 2018;80(S106).doi:10.1097/SAP.0000000000001351.
9. Sumit A, Suresh T, Garikipat A, et al. Modeling combined ultrasound and photoacoustic imaging: Simulations aiding device development and artificial intelligence. Photoacoustics 2021;24. doi:10.1016/j.pacs.2021.100304.
10. Warrier GS, Amirthalakshmi TM, Nimala K, et al. Automated recognition of cancer tissues through deep learning framework from the photoacoustic specimen. Contrast Media Molecular Imag 2022. doi: 10.1155/2022/4356744
11. Mohajerani P, Aguirre J, Omar M, et al. Machine-learning powered optoacoustic sensor for diabetes progression. Medrxiv. 2021. doi:10.1101/2021.03.17.21253779

12. Liakat S, Bors KA, Xu L, et al. Noninvasive in vivo glucose sensing on human subjects using mid-infrared light. Biomed Opt Express. 2014;5:2397–2404. doi: 10.1364/BOE.5.002397.

13. Sei K, Fujita M, Hirasawa T, et al. Measurement of blood-oxygen saturation using a photoacoustic technique in the rabbit hypoxemia model. J Clin Monitor Comput. 2018;33:269–279. doi: 0.1007/s10877-018-0166-8.

14. Nguyen DD, Pang JY, Madill C, et al. Effects of 445-nm laser on vessels of chick chorioallantoic membrane with implications to microlaryngeal laser surgery. Laryngoscope 2021;131. doi: 10.1002/lary.29354.

15. Friedmann D and Verma KK. Enhanced perception of deoxygenated hemoglobin for the visualization of lower-extremity reticular veins. Dermatol Surg 2024;50(2):207–209. doi: 10.1097/DSS.0000000000003974.

16. Azizah RN, Puspitasari A and Lestari I. Relationship of carboxyhemoglobin (CoHb) and hemoglobin (Hb) levels in active smokers in gresik regency. Internat J Adv Health Sci Technol 2024;4(1):8–11. doi: 10.35882/ijahst.v4i1.291.

17. Low BH, Lin YD, Huang BW, et al. Impaired microvascular response to muscle stretching in chronic smokers with type 2 diabetes. Frontier Bioengineerin Biotechnol: Section Biomechanics 2020;8. doi: 10.3389/fbioe.2020.00602.

18. Hashimoto H. Impaired Microvascular vasodilator reserve in chronic cigarette smokers: a study of post-occlusive reactive hyperemia in the human finger. Japan Circulat J 1994;58:29–33.